

A New Perspective for Dipolarization Front Dynamics: Electromagnetic Effects of Velocity Inhomogeneity

Dong Lin¹, Wayne A. Scales¹, Gurudas Ganguli², Xiangrong Fu³, Chris Crabtree², Erik Tejero², Yuxi Chen⁴, and Alex Fletcher²

¹Bradley Department of Electrical and Computer Engineering, Virginia Tech, Blacksburg, Virginia, USA.

²Naval Research Lab, Washington DC, USA.

³New Mexico Consortium, Los Alamos, NM, USA.

⁴Center for Space Environment Modeling, University of Michigan, Ann Arbor, MI, USA.

Key Points:

- Magnetotail DF contains a substantial velocity shear in the tangential electron drift.
- The sheared flow is susceptible to the EIH instability and can broaden the DF by emitting broadband LH waves.
- The EIH emissions become more electromagnetic as plasma beta increases.

This is the author manuscript accepted for publication and has undergone full peer review but has not been through the copyediting, typesetting, pagination and proofreading process, which

may lead to differences between this version and the Version of Record. Please cite this article as doi: [10.1029/2019JA026815](https://doi.org/10.1029/2019JA026815)

Abstract

The stability of a quasi-static near-Earth dipolarization front (DF) is investigated with a two-dimensional electromagnetic particle-in-cell (EMPIC) model. Strongly localized ambipolar electric fields self-consistently generates a highly sheared downward $\vec{E} \times \vec{B}$ electron drift on the kinetic scale in the DF. EMPIC simulations based on the observed DF thickness and gradients of plasma/magnetic field parameters reveal that the DF is susceptible to the kinetic electron-ion hybrid (EIH) instability driven by the strong velocity inhomogeneity. The excited waves show a broadband spectrum in the lower hybrid (LH) frequency range, which has been often observed at DFs. The wavelength is comparable to the shear scale length and the growth rate is also in the LH frequency range, which are consistent with the EIH theory. As a result of the LH wave emissions, the velocity shear is relaxed and the DF is broadened. When the plasma beta increases, the wave mode shifts to longer wavelengths with reduced growth rates and enhanced magnetic fluctuations although the wave power is mostly in the electrostatic regime. This study highlights the role of velocity inhomogeneity in the dynamics of DF which has been long neglected. The EIH instability is suggested to be an important mechanism for the wave emissions and steady-state structure at the DF.

1 Introduction

Dipolarization fronts (DFs) are Earthward propagating boundary layer structures that are frequently observed in the Earth's magnetotail. The most prominent feature of DFs is a sharp increase of magnetic field northward component over a scale length comparable to or less than the ion thermal gyroradius [Runov *et al.*, 2009, 2011]. DFs are generally believed to be generated by magnetotail reconnection. When the hot and tenuous reconnection jet encounters the denser and colder ambient magnetotail plasma, the kinetic scale boundary layer is formed [e.g., Sitnov *et al.*, 2009; Lu *et al.*, 2015]. The inhomogeneities of plasma and magnetic field parameters at DFs are expected to excite a number of wave modes. Waves with a broad frequency range are observed to coincide with the DF, with frequencies extending from below the lower hybrid (LH) frequency to above the electron cyclotron frequency [e.g., Zhou *et al.*, 2009].

The strong Earthward density gradient at DFs has been shown to drive a hierarchy of instabilities on different scales. Runov *et al.* [2011] revealed that the plasma density typically decreases by $\sim 50\%$ at the tailward side of DF. Lapenta and Bettarini [2011] found with 3D magnetohydrodynamic (MHD) simulations that the density gradient at the DFs can lead to an interchange instability, the scale of which is selected by the kinking flux ropes upstream. Pritchett and Coroniti [2010] found with 3D electromagnetic particle-in-cell (EMPIC) simulations that the dipolarized plasma sheet configuration is unstable to a ballooning/interchange type mode, which has a wavelength on the order of the ion gyroradius. This mode can be interpreted as the low-frequency extension of the lower hybrid drift instability (LHDI). The evolution of LHDI at DF has also been investigated by Divin *et al.* [2015a,b]. It was found that the density gradient driven LHDI generates wave modes on the electron gyroradius scale with frequencies in the LH range [Krall and Liewer, 1971].

The anisotropic velocity distributions are another energy source of unstable modes at the magnetotail DFs. Fu *et al.* [2012a] examined the pitch angle distribution of suprathermal electrons in the flux pileup regions (FPRs) located behind the DFs. They found perpendicular ($T_{\perp,e}/T_{\parallel,e} > 1$) and parallel ($T_{\perp,e}/T_{\parallel,e} < 1$) distributions inside the growing and decaying FPRs, respectively. These distributions are suggested to result from betatron acceleration due to the magnetic field compression and Fermi acceleration due to the shrinkage of a flux tube [Fu *et al.*, 2011; Huang *et al.*, 2015; Lu *et al.*, 2016b], and could drive the temperature anisotropy whistler instability and oblique electron firehose instability, respectively [Zhang *et al.*, 2018].

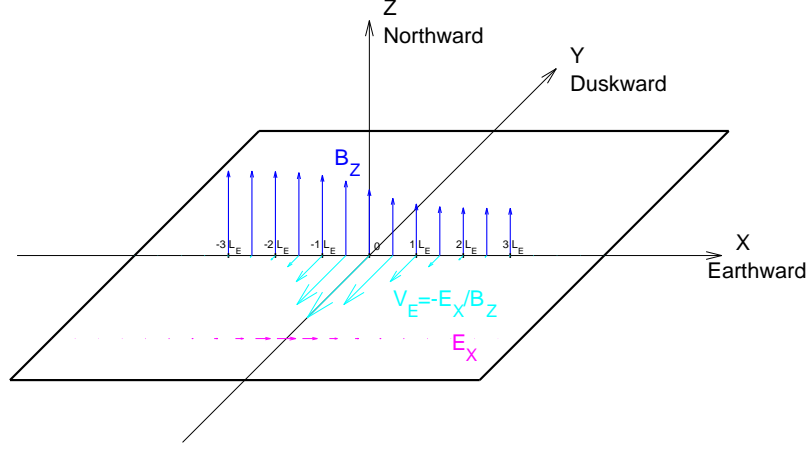
While the density gradient and anisotropy driven instabilities have been investigated in a number of studies, the effects of flow inhomogeneity within the DF has been long neglected. The strong gradient of magnetic field B_Z at DFs implies the existence of a current density in the dusk direction, which has been verified by satellite observations [e.g. *Fu et al.*, 2012b]. The current density was shown to be mainly carried by the dawnward drifting electron flow, which consists of both diamagnetic drift due to electron pressure gradient, and the $\vec{E} \times \vec{B}$ drift due to the Earthward electric field. Note here the ions are effectively unmagnetized in the DF thus can not undergo the drift motion entirely [*Ganguli et al.*, 2018] [*Wu and Shay*, 2012]. The transverse electric field is essentially an Earthward ambipolar electric field due to the global compression effects and localized in the DF. Further quantitative analysis reveal that the $\vec{E} \times \vec{B}$ drift is dominant over the diamagnetic drift, and ion flow is relatively negligible [*Fu et al.*, 2012b; *Fletcher et al.*, 2019]. Considering the kinetic scale thickness, the electron flows within the DFs are shown to have a substantial velocity shear, the electromagnetic effects of which on the DF stability, however, have not been well explored before [*Ganguli et al.*, 2018; *Fletcher et al.*, 2019].

Velocity shear driven instabilities are ubiquitous in space plasma environments on different scales. Depending on the shear scale length L_E relative to the ion gyroradius ρ_i , the consequent wave modes have different wave frequencies and wavelengths that are commensurate with the velocity shear [*Ganguli et al.*, 1994a,b]. The classical Kelvin-Helmholtz instability (KHI) is in the fluid regime $L_E \gg \rho_i$, which can be observed on e.g., the Earth's magnetopause [*Hasegawa et al.*, 2004]. The wave frequency is much less than the ion gyro frequency Ω_{ci} , and the wavelength is much longer than ρ_i [*Lin et al.*, 2014]. Kinetic theories have been developed to characterize the unstable wave modes when L_E is comparable to or smaller than ρ_i . Specifically, the electron-ion hybrid (EIH) instability is driven by the transverse velocity shear with intermediate scale length ($\rho_e < L_E < \rho_i$), when ions are effectively unmagnetized and electrons have shear corrected velocity distributions [e.g., *Ganguli et al.*, 1988a,b; *Romero et al.*, 1992]. The kinetic EIH modes have been verified in a number of space and laboratory experiments and numerical simulations [e.g., *Scales et al.*, 1994a,b; *Amatucci et al.*, 1996; *DuBois et al.*, 2014; *Liu et al.*, 2014, 2017; *Romero and Ganguli*, 1993], and are suggested to be important mechanisms for the generation of broadband electrostatic fluctuations. However, previous EIH studies have been mostly focused on the electrostatic emissions and assumed uniform magnetic field for simplicity [e.g., *Romero et al.*, 1992; *Romero and Ganguli*, 1993]. EIH modes in a more realistic configuration of a DF with magnetic gradient and their nonlinear electromagnetic properties have not been well understood.

Recently, *Ganguli et al.* [2018] showed with high-resolution Magnetospheric Multi-Scale (MMS) measurements that the ambipolar potential across the DF results in strongly sheared electron flows with sub-ion scale. *Liu et al.* [2018] reported MMS observation of an electron jet inside a DF that has a shear frequency larger than the lower hybrid frequency. *Fletcher et al.* [2019] investigated two DF events observed by the MMS satellite and developed a rigorous kinetic equilibrium. It still remains unclear how the highly sheared tangential flow may contribute to the distinctive broadband emissions at DFs. In this study, we evaluate the role of the velocity shear at DFs by investigating the excitation of the electromagnetic EIH instability [*Ganguli et al.*, 2014] at a kinetic scale boundary layer with sharp gradients of magnetic and plasma parameters. Electromagnetic particle-in-cell simulations are conducted to explore the DF stability and consequent spectral characteristics.

2 Model Configuration

Figure 1 shows the configuration of transverse sheared flows in a magnetotail DF structure. The magnetic field at the DF is characterized by enhanced northward component B_Z with a tailward gradient. An Earthward ambipolar electric field E_X is localized within the front due to the compression of magnetotail reconnection outflow, which drives



113 **Figure 1.** Transverse sheared electron flow in the equatorial plane of a DF. The blue arrows show the north-
 114 ward magnetic field B_Z with a tailward gradient. The magenta arrows show the Earthward ambipolar electric
 115 field. The cyan arrows show the dawnward drift velocity of electron.

120 $\vec{E} \times \vec{B}$ drift flow toward the dawn. The gradient scale length of the DF is chosen to be
 121 intermediate between the ion and electron gyroradius so that ions are effectively unmagne-
 122 tized within the DF while electrons are magnetized. The dawnward $\vec{E} \times \vec{B}$ drift and dia-
 123 magnetic drift of electrons result in a net current density toward the duskside. Although
 124 we choose a DF in the equatorial plane, our approach is valid to off equatorial DFs as
 125 long as the criterion that the scale size normal to the DF (of the order of an ion gyroradi-
 126 us) is much smaller than in the other orthogonal directions (of the order of several Earth
 127 radii). As explained in Ganguli et al. [2018], under this condition the physics in the normal
 128 direction is only weakly coupled to the other orthogonal directions and the problem
 129 essentially reduces to 1D as far as the kinetic and fast processes, such as wave generation
 130 in and around the lower hybrid frequency, are concerned. The model we used for simu-
 131 lation is consistent with the fully kinetic treatment but easier to implement. However, for
 132 slow MHD scale processes other dimensions are important as well.

133 In this study, we adopt a force-balanced model by assuming the ambipolar electric
 134 field is localized in the DF and the density profile has a smooth transition of hyperbolic
 135 tangent form. The force balance is achieved between the pressure gradient force, $\vec{J} \times \vec{B}$
 136 force, and the electric force. The B_Z profile can be then determined from Ampere's Law.
 137 This is a simplified representation of the fully kinetic model in the strong shear region.
 138 As explained in Ganguli et al. [2018] and Fletcher et al. [2019], there are stronger gradi-
 139 ents on the order of a few electron gyroradius within the DF. These are the likely regions
 140 where the waves will first emerge and hence we simulate this region. Within this region
 141 $\rho_e \ll L_E \ll \rho_i$ and the the electric field may be modeled by Equation (1) and the density
 142 gradient by Equation (2). Equation (3) is the Maxwell equation which leads to the mag-
 143 netic field pileup as shown in Equation (4).

$$E_X(x) = E_m \operatorname{sech}^2 \frac{x}{L_E} \quad (1)$$

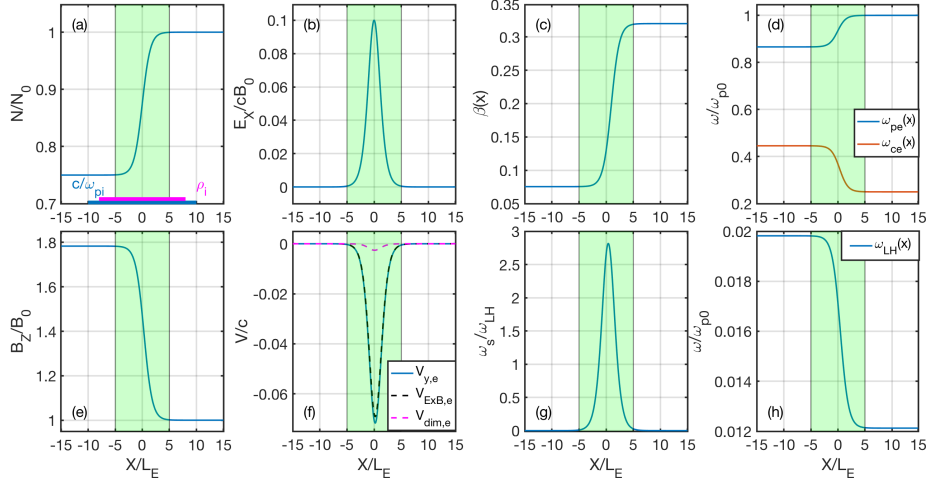
$$N(x) = N_0 \left[1 + \frac{\Delta N}{2} \left(\tanh \frac{x}{L_E} - 1 \right) \right] \quad (2)$$

$$\nabla \times \vec{B} = \mu_0 N e q_e (\vec{V}_{dim} + \vec{V}_{\vec{E} \times \vec{B}}) \quad (3)$$

$$B_Z(x) = B_0 \sqrt{1 + \beta_0 \left(1 - \frac{N(x)}{N_0} \right) + \frac{N_0}{\Delta N} \frac{e E_m L_E}{B_0^2 / 2 \mu_0} \left[1 - \left(\frac{N(x)}{N_0} \right)^2 \right]} \quad (4)$$

144 Here E_X is the Earthward ambipolar electric field. $N(x)$ is the distribution of ion number
 145 density along the X direction. B is the northward magnetic field along the Z direction.

146 $B_Z(x)$ is the magnetic field distribution along the X direction derived from Ampere's Law.
 147 L_E is the shear scale length. E_m is the peak value of the electric field. N_0 , B_0 , and β_0 are
 148 the number density, magnetic field, and electron plasma β Earthward of DF, respectively.
 149 ΔN is the ratio of density drop from Earthward to tailward relative to N_0 . N_e is the elec-
 150 tron number density which is approximately equal to the ion number density and satisfies
 151 Gauss' Law. μ_0 is the magnetic permeability in vacuum. q_e is the electric charge of an
 152 electron. \vec{V}_{dim} is the diamagnetic drift velocity of electrons: $\frac{-\nabla P_e \times \vec{B}}{N_e q_e B^2}$. $\vec{V}_{\vec{E} \times \vec{B}}$ is the $\vec{E} \times \vec{B}$
 153 drift velocity of electrons: $\frac{\vec{E} \times \vec{B}}{B^2}$. The two drifts represent the electron responses to differ-
 154 ent driving forces, which affect the wave generation differently especially when the gradi-
 155 ent scale size becomes of the order of an ion gyroradius or less [Fletcher et al. 2019].



156 **Figure 2.** Initial profiles of (a) plasma density, (b) electric field E_X , (c) plasma β , (d) electron plasma fre-
 157 quency ω_{pe} (blue) and electron cyclotron frequency ω_{ce} (orange), (e) magnetic field B_Z , (f) electron total
 158 drift velocity (blue), $\vec{E} \times \vec{B}$ drift (black dash), and diamagnetic drift (magenta), (g) ratio between shear fre-
 159 quency ω_s and the lower hybrid frequency ω_{LH} , (h) lower hybrid frequency ω_{LH} . The green shaded regions
 160 show the DF thickness represented by the transitions of electromagnetic/plasma parameters.

161 Figure 2 shows the initial profiles of the plasma parameters and electromagnetic
 162 field components in the DF model. The X axis is pointing toward the Earth. The values
 163 are derived from the observed event in *Ganguli et al. [2018]* but have been adapted to
 164 accommodate the simulation capacity. Figure 2(a) and (e) show the plasma density and
 165 magnetic field B_Z , which both use the values on the Earthward side as units. The plasma
 166 density has an Earthward gradient and drops by 25% tailward of the DF. B_Z increases to
 167 about $1.8 B_0$ in the tailward direction as a result of force balance. Note in the observation,
 168 the tailward B_Z is about $1.9 B_0$ (from ~ 7 nT to ~ 13 nT). This can be seen as the mag-
 169 netic field generated by the $\vec{E} \times \vec{B}$ drifting electrons with nearly stationary ions because of
 170 negligible gyro-averaged ion $\vec{E} \times \vec{B}$ drift due to the small scale electric field. Figure 2 (b)
 171 and (f) show the ambipolar electric field E_X and the electron dawnward drift velocities.
 172 The E_X has a peak value of $E_m = 0.1cB_0$. Here c is the light speed. The electron ve-
 173 locity is dominated by the $\vec{E} \times \vec{B}$ drift, with peak magnitude $0.069c$. The peak magnitude
 174 of the diamagnetic drift is $0.003c$. Figure 2 (c) shows the electron plasma $\beta_e = \frac{NkT_0}{B_Z^2/2\mu_0}$
 175 varies from 0.08 in the tailward to 0.32 in the Earthward regions. Note $\beta_e = 0.6$ in the
 176 observation of *Ganguli et al. [2018]*. Here the ion and electron temperatures are assumed
 177 to be uniform for simplicity, i.e. neither ion nor electron temperatures have spatial gra-
 178 dient. Figure 2 (g) shows the ratio between the shear frequency $\omega_s = V_{y,e}/L_E$ and describes the in-
 179

180 homogeneity of the electron flow. Here the ratio ω_s/ω_{LH} is up to 3 within the unstable
 181 range. The electron plasma frequency $\omega_{pe} = \sqrt{\frac{Ne^2}{\epsilon_0 m_e}}$ and electron cyclotron frequency
 182 $\omega_{ce} = \frac{eB_z}{m_e}$ are shown in Figure 2 (d) in blue and orange, respectively. The lower hybrid
 183 frequency $\omega_{LH} = \frac{\omega_{pi}}{\sqrt{1+(\frac{\omega_{pe}}{\omega_{ce}})^2}}$ is shown in Figure 2 (h). The three frequencies are shown in
 184 unit of the electron plasma frequency $\omega_{p0} = \sqrt{\frac{N_0 e^2}{\epsilon_0 m_e}}$ Earthward of the DF.

185 In this study, we use an electron thermal speed of $V_{the} = 0.1c$ and ion/electron tem-
 186 perature ratio of 4: $T_e = T_i/4 = T_0$. The ratio between electron plasma frequency and
 187 gyro frequency on the Earthward side is $\omega_{pe}/\omega_{ce} = 4$. A reduced mass ratio between ion
 188 and electron is assumed $m_i/m_e = 400$. The ion and electron gyroradius on the Earthward
 189 side are $\rho_i = 16c/\omega_{pe}$ and $\rho_e = 0.4c/\omega_{pe}$, respectively. Here we choose the initial value
 190 of $L_E = 1.5c/\omega_{pe} = \rho_i/10.67 = 3.75\rho_e$ in the simulation so that ions can be effec-
 191 tively unmagnetized and electrons magnetized. The green shaded boxes in Figure 2 show
 192 the transition regions of the electromagnetic and plasma parameter profiles, which provide
 193 a rough estimation of the DF thickness as was used in observational analysis [e.g. *Runov*
 194 *et al.*, 2011; *Schmid et al.*, 2011]. Note that the initial DF thickness is $\sim 10 c/\omega_{pe}$ con-
 195 sidering the hyperbolic function form, and that the observed DF thickness is related to the
 196 saturated status of the instability. The DF thickness in this simulation is basically compa-
 197 rable to the ion scale length and consistent with observations [e.g. *Fu et al.*, 2012b; *Gan-*
 198 *guli et al.*, 2018; *Liu et al.*, 2018]. The Alfvén speed based on B_0 and N_0 is $V_{A0} = 0.25c$.

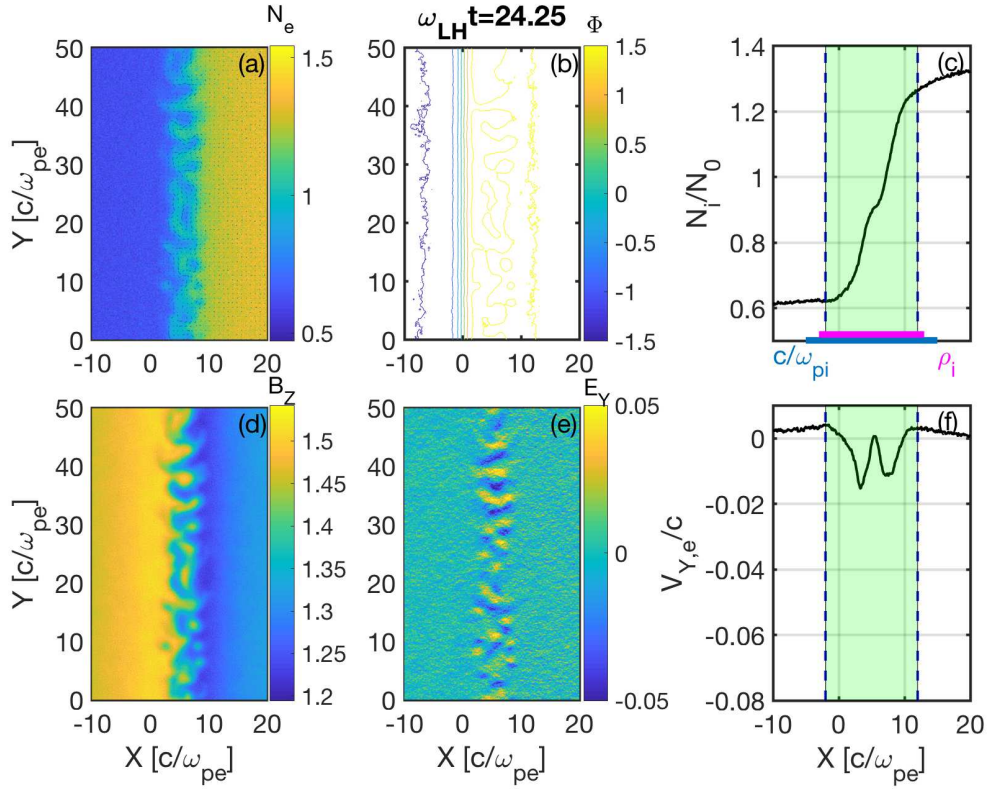
199 The EMPIC model we used is two-dimensional in the configuration space with three
 200 velocity components (2D3V). Both ions and electrons are fully kinetic, and the full set of
 201 Maxwell's equations are solved. In order to make use of the periodic boundary conditions,
 202 the simulation domain is doubled in the X direction and made symmetric about $x = L_X/2$.
 203 The system length is $L_X = 100c/\omega_{pe}$ and $L_Y = 50c/\omega_{pe}$ with $N_X \times N_Y = 1024 \times 512$
 204 grid cells. The mean number of macro-particles per cell per species is 200. The time step
 205 is $0.01\omega_{p0}^{-1}$. Since the LH time scale is the natural time scale in the system, we use ω_{LH0}^{-1}
 206 as the unit where ω_{LH0} is the LH frequency Earthward of the DF.

207 3 Simulation Results

208 3.1 EIH Wave Spectrum

209 Figure 3 shows the plasma density, electron velocity, and electromagnetic fields
 210 at $t=24.25 \omega_{LH0}^{-1}$ when the instability has evolved into the nonlinear stage. Figure 3 (a)
 211 shows rolled-up vortex structuring in the electron number density (N_e), which is charac-
 212 teristic of the EIH instability [*Romero and Ganguli*, 1993]. Figure 3 (b), (d), and (e) show
 213 coherent structures in the electrostatic potential Φ , B_z , and E_y . A rough estimation of
 214 the dominant wavelength is $4.2c/\omega_{pe}$, which is comparable to the shear scale length. Fig-
 215 ure 3 (c) and (f) show that the ion number density (N_i) still maintains a strong gradient
 216 while the electron sheared flow ($V_{y,e}$) has been mostly depleted. The saturated DF layer
 217 is broadened to $\sim 14 c/\omega_{pe} = 0.7 c/\omega_{pi} = 0.9 \rho_i$, which is consistent with observations.
 218 Note the flow channel has a displacement along X due to the net magnetic gradient force
 219 as the ambipolar electric field is depleted by the instability.
 220
 221
 222

223 In order to further characterize the wave modes, we sample the transverse electric
 224 field perturbation of E_y along the flow channel in the DF. The time history of the one-
 225 dimensional sampling is shown in Figure 4 (a). It can be seen that periodic wave struc-
 226 tures start to show up at $\sim 3\omega_{LH}^{-1}$. The wave fronts represented by the alternating strips
 227 indicate that the wave mode is propagating along the Y positive axis toward the dusk. The
 228 phase velocity estimated from the slope of the wave front is $\sim 0.004c$, which is compar-
 229 able to the ion thermal velocity.
 230
 231
 232
 233

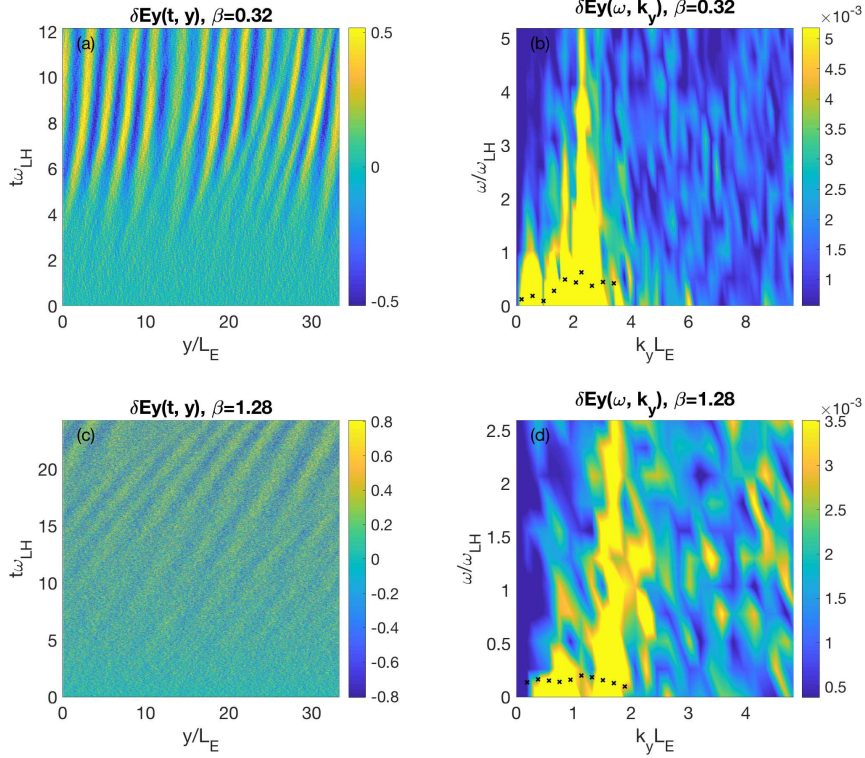


209 **Figure 3.** Plasma and electromagnetic field variables at $t=24.25 \omega_{LH0}^{-1}$: (a) electron number density N_e , (b)
 210 electrostatic potential Φ , (c) cross section of ion density N_i , (d) B_z , (e) E_y , and (f) cross section of electron
 211 flow $V_{y,e}$.

234 A two-dimensional Fourier analysis is applied to the space-time sampling of electric
 235 field perturbations shown in Figure 4 (a). The consequent dispersion relation is shown in
 236 Figure 4 (b). It can be seen that the dominant wave number is around $k_y L_E = 2$ and
 237 the frequency is broadband from 0 to $5\omega_{LH}$. At each sampled time, a spatial Fourier
 238 analysis is conducted to get the spectrum power of different wave numbers. The time history of
 239 the spectrum power for one k_y mode is linearly fitted to estimate the growth rate of that
 240 mode. The growth rates of a few wave modes around the dominant mode are indicated
 241 by the black crosses shown in Figure 4 (b). It can be seen that the fastest growth rate is
 242 also on the order of the lower hybrid frequency. The dispersion relation shown in Figure
 243 4 (a-b) is consistent with the EIH theory that the fastest growing mode has a wavelength
 244 comparable to the shear scale length, the real frequency is broadband in the lower hybrid
 245 range, and the fastest growing mode has a growth rate comparable to the lower hybrid
 246 frequency [Romero *et al.*, 1992].

247 3.2 EIH Dependence on Plasma β

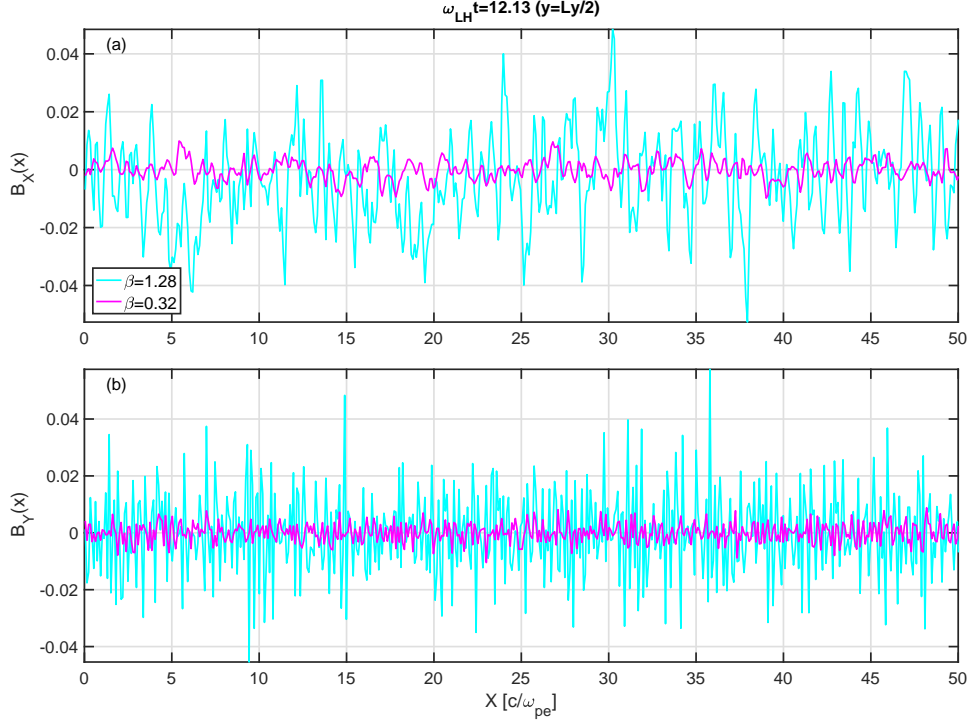
248 We also explored the wave properties dependence on the plasma β . Another simulation
 249 was conducted in which the plasma thermal velocity is increased by a factor of
 250 two so that the plasma β in the Earthward direction is 1.28. The density gradient, driving
 251 electric field, and shear scale length are kept the same. The maximum B_z at the tailward
 252 direction is slightly increased from $1.78B_0$ to $1.85B_0$. The wave structure and dispersion



223 **Figure 4.** Wave mode characterization. (a-b) Time history of E_Y perturbation sampled along the flow di-
 224 rection in the DF, and the dispersion relation of the sampled E_Y . The black crosses indicate the growth rates
 225 of each k_y mode. (c-d) sampled E_Y perturbation time history and its dispersion relation for another test of
 226 $\beta = 1.28$ in the same format with (a-b).

253 properties in the DF are shown in Figure 4 (c-d) in the same format with Figure 4 (a-b).
 254 The wave pattern becomes visible after $\sim 10 \omega_{LH}^{-1}$ (Figure 4 c). The dispersion relation in
 255 Figure 4 (d) indicates that the lower hybrid spectrum shrinks to a lower frequency band.
 256 The fastest growing wave number shifts to smaller values around $k_y L_E \sim 1$. The growth
 257 rate is reduced as the plasma β is higher. This is consistent with the theory [Ganguli
 258 *et al.*, 2014] and observations of DF which indicate that the wave power is concentrated
 259 in the electrostatic regime.

263 The effects of plasma β are further evaluated by plotting the electromagnetic per-
 264 turbations from the two simulations with low and high plasma β . Figure 5 shows the B_X
 265 and B_Y sampled at $t = 12.13\omega_{LH}^{-1}$ and $y = L_Y/2$ along the X direction. The results from
 266 the high β simulation are shown in cyan and from the low β in magenta. The magnetic
 267 perturbations in the high β simulation has a much larger amplitude than those from the
 268 low β simulation. Considering that the background magnetic field is only different by 4%
 269 and that the high β case has much lower growth rate, the direct comparison of magnetic
 270 perturbations here imply that the fluctuations driven by the transverse velocity shear at the
 271 DF are more electromagnetic with a higher β .



260 **Figure 5.** Comparison of electromagnetic perturbations between low and high β . The magnetic field compo-
 261 nents (a) B_X and (b) B_Y sampled along the X direction at $Y = L_Y/2$ are shown for two runs: $\beta = 0.32$
 262 (magenta) and $\beta = 1.28$ (cyan).

272 4 Discussion and Conclusion

273 In this study, we investigated the velocity shear effects in the magnetotail dipolariza-
 274 tion front with a two-dimensional electromagnetic PIC model. A simplified configura-
 275 tion is adopted in which the DF is treated as a boundary layer with an Earthward plasma den-
 276 sity gradient, a tailward magnetic field B_Z gradient, and an Earthward ambipolar elec-
 277 tric field E_X . The velocity shear mainly results from the inhomogeneous electric field
 278 which represents the global compression effects. The particle distribution is deviated from
 279 Maxwellian, which provides the free energy for the EIH wave emission.

280 It should be pointed out that the EIH mechanism is different from the LHDI. Firstly,
 281 the energy source of EIH instability is the velocity shear while the LHDI is driven by den-
 282 sity gradient. The EIH does not require a density gradient (Figure 3c) but depletes the
 283 velocity shear and relaxes the DF (Figure 3f) [Romero *et al.*, 1992]. This may explain why
 284 DF electron jets are not commonly reported although a statistical survey is needed to evalu-
 285 ate the occurrence. Secondly, the saturated EIH state is featured by vortex structure (Fig-
 286 ure 3a), distinct from the “finger” structures of LHDI [Pritchett and Coroniti, 2010; Divin
 287 *et al.*, 2015a]. On the other hand, uniform $\vec{E} \times \vec{B}$ drift velocity is typically assumed for
 288 the study of the LHDI [e.g., Daughton, 2003]. This may be problematic for DF studies
 289 since when the scale size of the density gradient becomes comparable to an ion gyroradius
 290 (as typically found in DFs) the assumption of uniform drift does not hold [Ganguli *et al.*,
 291 2018].

292 The DF thickness in the simulations presented in this study is representative of
 293 the ion scale length as has been found in observations [e.g., Runov *et al.*, 2009, 2011;
 294 Schmid *et al.*, 2011; Fu *et al.*, 2012b; Liu *et al.*, 2018; Ganguli *et al.*, 2018]. Note that the

DF thickness in observations are usually estimated with the timing method. This method derives the propagation velocity of the DF based on two or more satellites that are close enough to each other, and estimates the duration of DF passing with the local minimum and maximum of the magnetic field profile. The DF thickness is then estimated as the product of the propagation velocity and duration time. In this simulation study, the model is set in the frame of the DF thus there are no propagation effects. The magnetic profile is simplified with a hyperbolic tangent like function, thus there are no local maximum or minimum. Instead, the DF thickness is estimated with the distance between the asymptotic points of the profile. It should be clarified that the shear scale length L_E used in this initialization is $1.5 c/\omega_{pe}$, which is equivalent to $0.075 c/\omega_{pi}$. However, the DF thickness based on the method typically used in observations is about $10 c/\omega_{pe}$, as shown by the green shaded boxes in Figure 2. This thickness is equivalent to $0.5 c/\omega_{pi}$ or $0.6 \rho_i$, as shown by the blue and magenta bars in Figure 2, respectively. The DF thickness is broadened as a result of the wave emission driven by the EIH instability. As shown in Figure 3 (c), the DF thickness has increased to $\sim 14 c/\omega_{pe}$ by $24.25 \omega_{LH0}^{-1}$, which is equivalent to $0.7 c/\omega_{pi}$ or $0.9 \rho_i$. Here c/ω_{pi} and ρ_i are both based on the initial values Earthward of the DF. Considering that the Earthward density increased slightly by $24.25 \omega_{LH0}^{-1}$, the actual ion inertial length is smaller than the value at initialization and closer to the DF thickness.

The simulation was run for $24.25\omega_{LH}^{-1}$ or equivalently $1.25\Omega_{ci}^{-1}$, when the saturated states still hold. In another run that is not shown here, the initial shear scale length is doubled ($L_E = 3.0c/\omega_{pe}$). The electron flow channel width is broadened to $1.9\rho_i$ or equivalently $1.5c/\omega_{pi}$. Although the shear frequency is lower than that in the simulation presented here, the EIH instability still develops very well. We present the results for $L_E = 1.5c/\omega_{pe}$ because the physics is similar while the computation is simpler considering that the system length needs to be commensurate with the shear scale length. It is also noteworthy that the flow channel in the saturated stage is shifted in the direction transverse to the flow, which is caused by the force balance. As the electron flow is depleted, the magnetic gradient force compresses the DF, which results in the Earthward displacement of the initial DF.

Uniform electron and ion temperatures are used in this simulation study although the temperatures typically have a gradient across the DF in satellite observations and self-consistently formed DFs [e.g. *Runov et al.*, 2009, 2011; *Lu et al.*, 2016a]. However, the temperature gradient in the MMS observation of DF reported by *Ganguli et al.* [2018] is negligible. This event is used in our simulation because its equilibrium physics is thoroughly analyzed thus provides a firm basis to study the nonlinear evolution. On the other hand, the temperature gradient in DF is usually found to be in the opposite direction to the density gradient, which reduces the pressure gradient and hence the diamagnetic drift but not the ambipolar electric field driven $\vec{E} \times \vec{B}$ drift. This will further enhance the EIH waves and retard the lower hybrid drift or other pressure gradient driven waves.

The higher plasma β in the study of EIH dependence on β is achieved by increasing the temperature of electrons and ions while keeping the other parameters such as the shear scale length L_E the same. The challenge of using a larger β in the simulation is that the shear scale length and the system length have to increase accordingly with the electron/ion gyro radius while the electron gyroradius has to be resolved to achieve the $\vec{E} \times \vec{B}$ drift motion. Considering that DF thickness is usually comparable to the ion gyroradius, a larger plasma β may imply a thicker DF boundary layer thus a lower shear frequency. Here we control the variables such as L_E to highlight that with increasing β the wavelengths of the EIH waves become longer and they become increasingly electromagnetic. This is important since although the power in DF emission is mostly in the electrostatic regime there is also some power in the electromagnetic regime. The velocity shear generated EIH waves display this character. This has important physics implications since it implies that most of the energy goes into particle energization in the DF frame as the electrostatic power dissi-

348 pates rather than be transported away from the DF as Poynting flux by the electromagnetic
349 waves.

350 When the DFs are propagating toward the Earth, there is a convection electric field
351 along the dusk direction. In this study, the EIH instability is investigated in the reference
352 frame moving with the DF thus there is no convection electric field in the dawn-dusk di-
353 rection. The ambipolar electric field along the X direction is not affected by the Earthward
354 motion.

355 The DF configuration adopted in this simulation is simplified however it retains the
356 critical aspects of the DF. A three-dimensional PIC model starting from magnetotail cur-
357 rent sheet configuration may provide a global view of the DF that is self-consistently gen-
358 erated from the magnetotail reconnection with Earthward propagation effects. However,
359 the EIH mechanism discussed in this study is essentially on the kinetic scale and a locally
360 dissipative process. It requires resolving the electron-ion charge separation scale and time
361 scale much below the ion gyro period. A local electromagnetic PIC model is sufficient for
362 such a purpose. Achieving such resolution in a global PIC model is still not practical.

363 This study provides the first electromagnetic kinetic simulation of the local dissipa-
364 tion in DF due to velocity inhomogeneities. It is highlighted that the velocity shear sub-
365 stantially contributes to the wave emissions at the magnetotail dipolarization fronts. The
366 EIH mechanism is suggested to be responsible for the generation of broadband lower hy-
367 brid waves at DFs. The transition of the EIH instability to more electromagnetic fluctua-
368 tions with increasing plasma β implies that the waves with more electromagnetic proper-
369 ties could propagate away from the DF and may affect other magnetospheric particle pop-
370 ulations. The shear driven wave modes have implications for the energy dissipation and
371 particle dynamics at the DF. Recent theoretical advances show that the EIH driven waves
372 are formally electromagnetic especially when the wave vector has a finite parallel compo-
373 nent [Ganguli *et al.*, 2014]. In order to fully characterize the electrostatic and electromag-
374 netic effects of the shear driven emissions at the DF, it is necessary to extend the current
375 2D model to 3D and global model and consider a broader range of plasma parameters in
376 the future. Whistler mode waves are also suggested to be excited by the velocity shear
377 when there is a finite parallel component of wave vector [Ganguli *et al.*, 2014]. Since the
378 magnetic field enhancement at DFs is often preceded by a decrease [e.g., Liu *et al.*, 2013;
379 Shi *et al.*, 2014; Lu *et al.*, 2016a], it is also necessary to consider how the DF-dip could
380 affect the particle distribution and velocity shear at the DF.

381 Acknowledgments

382 This study was funded by NASA MAG16_2-0050. The authors acknowledge Advanced
383 Research Computing (ARC) at Virginia Tech and the Space Computer Center (SpaceCC)
384 of the Electrical and Computer Engineering Department for providing computational re-
385 sources and technical support that have contributed to the results reported within this pa-
386 per. The model outputs that are used in this paper are being preserved in a Virginia Tech
387 data repository and can be accessed publicly at their website (<https://computing.ece.vt.edu/~ldong7/>).

388 References

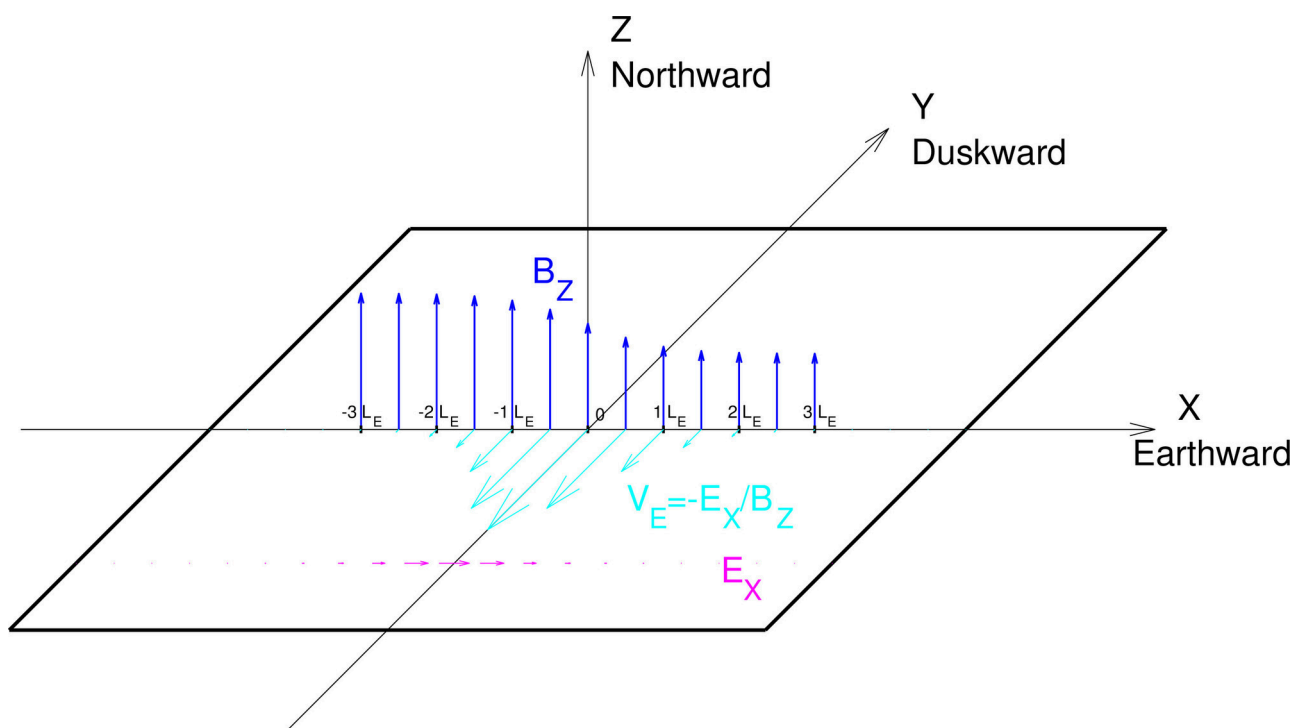
- 389 Amatucci, W. E., D. Walker, G. Ganguli, J. Antoniadis, D. Duncan, J. Bowles, V. Gavri-
390 ishchaka, and M. Koepke (1996), Plasma response to strongly sheared flow, *Phys. Rev.*
391 *Lett.*, 77(10), 1978–1981, doi:10.1103/PhysRevLett.77.1978.
- 392 Daughton, W. (2003), Electromagnetic properties of the lower-hybrid drift instability in a
393 thin current sheet, *Phys. Plasmas*, 10(8), 3103–3119, doi:10.1063/1.1594724.
- 394 Divin, A., Y. V. Khotyaintsev, A. Vaivads, M. André, S. Markidis, and G. Lapenta
395 (2015a), Evolution of the lower hybrid drift instability at reconnection jet front, *J. Geo-*
396 *phys. Res.: Space Physics*, 120(4), 2675–2690, doi:10.1002/2014JA020503.

- 397 Divin, A., Y. V. Khotyaintsev, A. Vaivads, and M. André (2015b), Lower hybrid drift in-
398 stability at a dipolarization front, *J. Geophys. Res.: Space Physics*, *120*(2), 1124–1132,
399 doi:10.1002/2014JA020528.
- 400 DuBois, A. M., E. Thomas, W. E. Amatucci, and G. Ganguli (2014), Experimental charac-
401 terization of broadband electrostatic noise due to plasma compression, *J. Geophys. Res.:
402 Space Physics*, *119*(7), 5624–5637, doi:10.1002/2014JA020198.
- 403 Fletcher, A. C., C. Crabtree, G. Ganguli, D. Malaspina, E. Tejero and X. Chu (2019),
404 Kinetic Equilibrium and Stability Analysis of Dipolarization Fronts, *J. Geophys. Res.:
405 Space Physics*, *124*, 2010–2028, doi:10.1029/2018JA026433.
- 406 Fu, H. S., Y. V. Khotyaintsev, M. André, and A. Vaivads (2011), Fermi and betatron ac-
407 celeration of suprathermal electrons behind dipolarization fronts, *Geophys. Res. Lett.*,
408 *38*(16), doi:10.1029/2011GL048528.
- 409 Fu, H. S., Y. Khotyaintsev, A. Vaivads, M. André, V. Sergeev, S. Huang, E. Kronberg,
410 and P. Daly (2012a), Pitch angle distribution of suprathermal electrons behind dipo-
411 larization fronts: A statistical overview, *J. Geophys. Res.: Space Physics*, *117*(A12), doi:
412 10.1029/2012JA018141.
- 413 Fu, H. S., Y. V. Khotyaintsev, A. Vaivads, M. André, and S. Huang (2012b), Electric
414 structure of dipolarization front at sub-proton scale, *Geophys. Res. Lett.*, *39*(6), doi:
415 10.1029/2012GL051274.
- 416 Ganguli, G., Y. Lee, and P. Palmadesso (1988a), Kinetic theory for electrostatic waves due
417 to transverse velocity shears, *Phys. Fluids*, *31*(4), 823–838, doi:10.1063/1.866818.
- 418 Ganguli, G., Y. Lee, and P. Palmadesso (1988b), Electron–ion hybrid mode due to trans-
419 verse velocity shear, *Phys. Fluids*, *31*(10), 2753–2756, doi:10.1063/1.866982.
- 420 Ganguli, G., H. Romero and J. Fedder (1994a), Interaction between global MHD and ki-
421 netic processes in the magnetotail., *Washington DC American Geophysical Union Geo-
422 physical Monograph Series*, *84*, 135–148, doi:10.1029/GM084p0135.
- 423 Ganguli, G., M. J. Keskinen, H. Romero, R. Heelis, T. Moore, and C. Pollock (1994b),
424 Coupling of microprocesses and macroprocesses due to velocity shear: An application
425 to the low-altitude ionosphere, *J. Geophys. Res.: Space Physics*, *99*(A5), 8873–8889,
426 doi:10.1029/93JA03181.
- 427 Ganguli, G., E. Tejero, C. Crabtree, W. Amatucci, and L. Rudakov (2014), Generation
428 of electromagnetic waves in the very low frequency band by velocity gradient, *Phys.
429 Plasmas*, *21*(1), 012,107, doi:10.1063/1.4862032.
- 430 Ganguli, G., C. Crabtree, A. C. Fletcher, E. Tejero, D. Malaspina, and I. Cohen
431 (2018), Kinetic equilibrium of dipolarization fronts, *Sci. Rep-UK*, *8*(1), 17,186, doi:
432 10.1038/s41598-018-35349-9.
- 433 Hasegawa, H., M. Fujimoto, T.-D. Phan, H. Reme, A. Balogh, M. Dunlop, C. Hashimoto,
434 and R. TanDokoro (2004), Transport of solar wind into Earth’s magnetosphere through
435 rolled-up Kelvin-Helmholtz vortices, *Nature*, *430*(7001), 755.
- 436 Huang, C., M. Wu, Q. Lu, R. Wang, and S. Wang, et al. (2015), Electron acceleration
437 in the dipolarization front driven by magnetic reconnection, *J. Geophys. Res.: Space
438 Physics*, *120*(8), 1759–1765, doi:10.1002/2014JA020918.
- 439 Krall, N. A and P. C Liewer (2014), Low-frequency instabilities in magnetic pulses, *Phys.
440 Rev. A*, *4*(5), 2094–2103, doi:10.1103/PhysRevA.4.2094.
- 441 Lapenta, G., and L. Bettarini (2011), Self-consistent seeding of the interchange instability
442 in dipolarization fronts, *Geophys. Res. Lett.*, *38*(11), doi:10.1029/2011GL047742.
- 443 Lin, D., C. Wang, W. Li, B. Tang, X. Guo, and Z. Peng (2014), Properties of Kelvin-
444 Helmholtz waves at the magnetopause under northward interplanetary magnetic
445 field: Statistical study, *J. Geophys. Res.: Space Physics*, *119*(9), 7485–7494, doi:
446 10.1002/2014JA020379.
- 447 Liu, C. M., H. S. Fu, A. Vaivads, Y. V. Khotyaintsev, D. J. Gershman, K. J. Hwang, Z.
448 Z. Chen, D. Cao, Y. Xu, J. Yang and others (2018), Electron jet detected by MMS at
449 dipolarization front, *Geophys. Res. Lett.*, *45*(2), 556–564, doi:10.1002/2017GL076509.

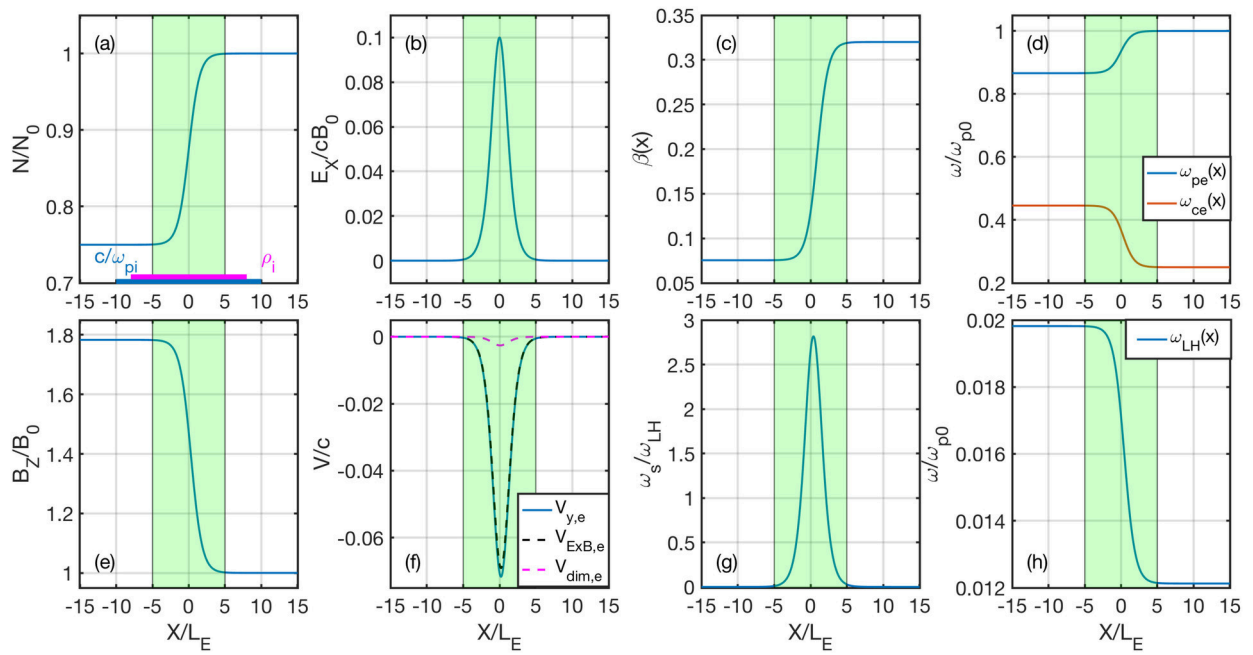
- 450 Liu, J., V. Angelopoulos, A. Runov, and X.-Z. Zhou (2013), On the current sheets sur-
 451 rounding dipolarizing flux bundles in the magnetotail: The case for wedgelets, *J. Geo-*
 452 *phys. Res.: Space Physics*, *118*(5), 2000–2020, doi:10.1002/jgra.50092.
- 453 Liu, Y., J. Cao, L. Xu, X. Zhang, P. Wang, J. Wang, Y. Du, and Z. Zheng (2014), Coher-
 454 ent structure generated in the boundary layer of a laboratory-created ionospheric deple-
 455 tion, *Geophys. Res. Lett.*, *41*(5), 1413–1419, doi:10.1002/2014GL059211.
- 456 Liu, Y., J. Lei, P. Yu, Z. Zhang, X. Zhang, and J. Cao (2017), Laboratory generation of
 457 broadband ELF waves by inhomogeneous plasma flow, *Geophys. Res. Lett.*, *44*(4), 1634–
 458 1640, doi:10.1002/2016GL072232.
- 459 Lu, S., Q. Lu, Y. Lin, X. Wang, Y. Ge, R. Wang, M. Zhou, H. Fu, C. Huang, M. Wu,
 460 et al. (2015), Dipolarization fronts as Earthward propagating flux ropes: A three-
 461 dimensional global hybrid simulation, *J. Geophys. Res.: Space Physics*, *120*(8), 6286–
 462 6300, doi:10.1002/2015JA021213.
- 463 Lu, S., A. Artemyev, V. Angelopoulos, Q. Lu, and J. Liu (2016a), On the current density
 464 reduction ahead of dipolarization fronts, *J. Geophys. Res.: Space Physics*, *121*(5), 4269–
 465 4278, doi:10.1002/2016JA022754.
- 466 Lu, S., V. Angelopoulos, and H. Fu (2016b), Suprathermal particle energization in dipolar-
 467 ization fronts: Particle-in-cell simulations, *J. Geophys. Res.: Space Physics*, *121*, 9483–
 468 9500, doi:10.1002/2016JA022815.
- 469 Pritchett, P., and F. Coroniti (2010), A kinetic ballooning/interchange instability in the
 470 magnetotail, *J. Geophys. Res.: Space Physics*, *115*(A6), doi:10.1029/2009JA014752.
- 471 Romero, H., and G. Ganguli (1993), Nonlinear evolution of a strongly sheared cross-field
 472 plasma flow, *Phys. Fluids B: Plasma Phys.*, *5*(9), 3163–3181, doi:10.1063/1.860653.
- 473 Romero, H., G. Ganguli, Y. Lee, and P. Palmadesso (1992), Electron–ion hybrid instabil-
 474 ities driven by velocity shear in a magnetized plasma, *Phys. Fluids B: Plasma Phys.*,
 475 *4*(7), 1708–1723, doi:10.1063/1.860028.
- 476 Runov, A., V. Angelopoulos, M. Sitnov, V. Sergeev, J. Bonnell, J. McFadden,
 477 D. Larson, K.-H. Glassmeier, and U. Auster (2009), THEMIS observations of
 478 an Earthward-propagating dipolarization front, *Geophys. Res. Lett.*, *36*(14), doi:
 479 10.1029/2009GL038980.
- 480 Runov, A., V. Angelopoulos, X.-Z. Zhou, X.-J. Zhang, S. Li, F. Plaschke, and J. Bonnell
 481 (2011), A THEMIS multicase study of dipolarization fronts in the magnetotail plasma
 482 sheet, *J. Geophys. Res.: Space Physics*, *116*(A5), doi:10.1029/2010JA016316.
- 483 Scales, W., P. Bernhardt, G. Ganguli, C. Siefiring, and P. Rodriguez (1994a), Small-scale
 484 plasma irregularities produced during electron attachment chemical releases, *Geophys.*
 485 *Res. Lett.*, *21*(7), 605–608, doi:10.1029/94GL00369.
- 486 Scales, W. A., P. Bernhardt, and G. Ganguli (1994b), Early time evolution of nega-
 487 tive ion clouds and electron density depletions produced during electron attachment
 488 chemical release experiments, *J. Geophys. Res.: Space Physics*, *99*(A1), 373–381, doi:
 489 10.1029/93JA02752.
- 490 Schmid, D. and Volwerk, M. and Nakamura, R. and Baumjohann, W. and Heyn, M.
 491 (2014), A statistical and event study of magnetotail dipolarization fronts, *Ann. Geophys.*,
 492 *29*(9), 1537–1547, doi:10.5194/angeo-29-1537-2011.
- 493 Shi, X., T. Chen, L. Zhang, S. Duan, J. Liu, and Z. He (2014), Ion flux dropout observed
 494 near dipolarization front, *Chinese Sci. Bull.*, *59*(34), 4790–4796, doi:10.1007/s11434-
 495 014-0616-8.
- 496 Sitnov, M., M. Swisdak, and A. Divin (2009), Dipolarization fronts as a signature of tran-
 497 sient reconnection in the magnetotail, *J. Geophys. Res.: Space Physics*, *114*(A4), doi:
 498 10.1029/2008JA013980.
- 499 Wu, P., and M. A. Shay (2012), Magnetotail dipolarization front and associated
 500 ion reflection: Particle-in-cell simulations, *Geophys. Res. Lett.*, *39*(L08107), doi:
 501 10.1029/2012GL051486.
- 502 Zhang, X., V. Angelopoulos, A. Artemyev, and J. Liu (2018), Whistler and electron fire-
 503 hose instability control of electron distributions in and around dipolarizing flux bundles,

504 *Geophys. Res. Lett.*, 45(18), 9380–9389, doi:10.1029/2018GL079613.
505 Zhou, M., M. Ashour-Abdalla, X. Deng, D. Schriver, M. El-Alaoui, and Y. Pang
506 (2009), THEMIS observation of multiple dipolarization fronts and associated wave
507 characteristics in the near-Earth magnetotail, *Geophys. Res. Lett.*, 36(20), doi:
508 10.1029/2009GL040663.

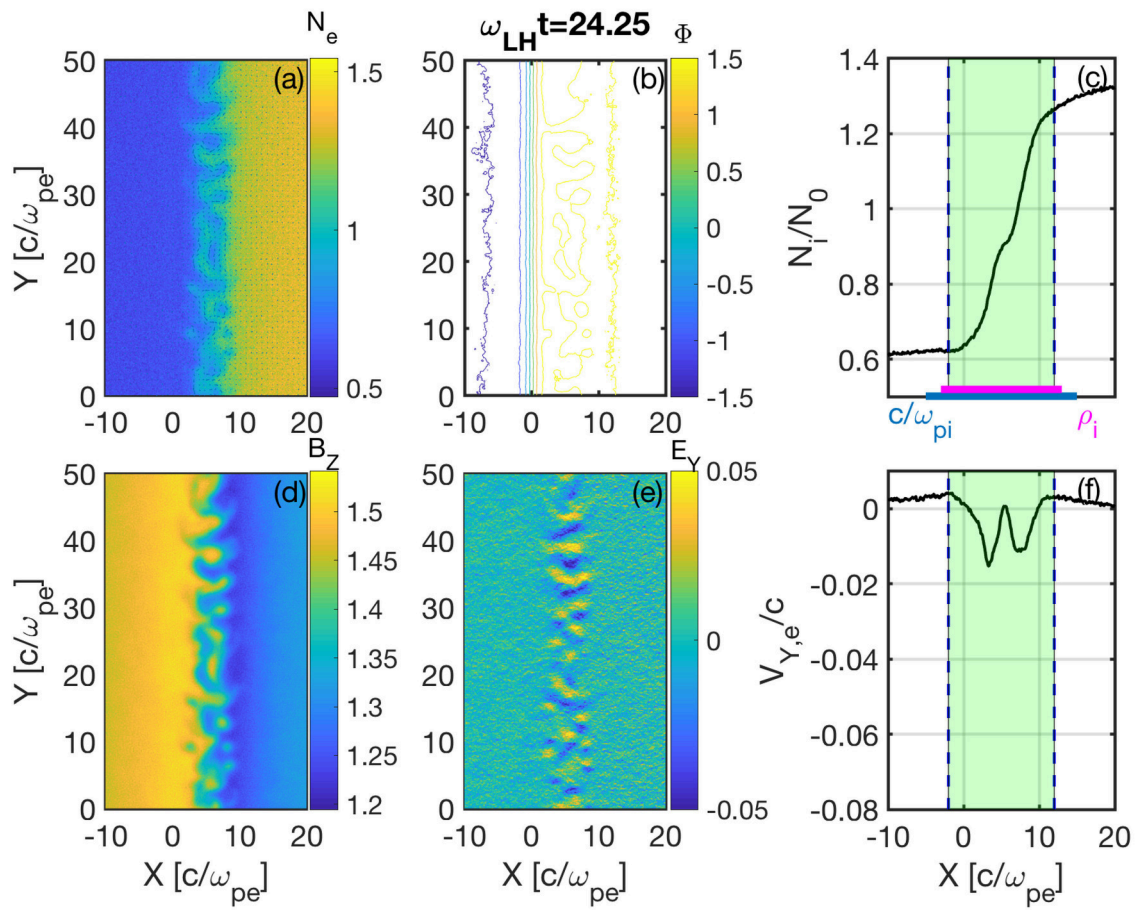
Author Manuscript



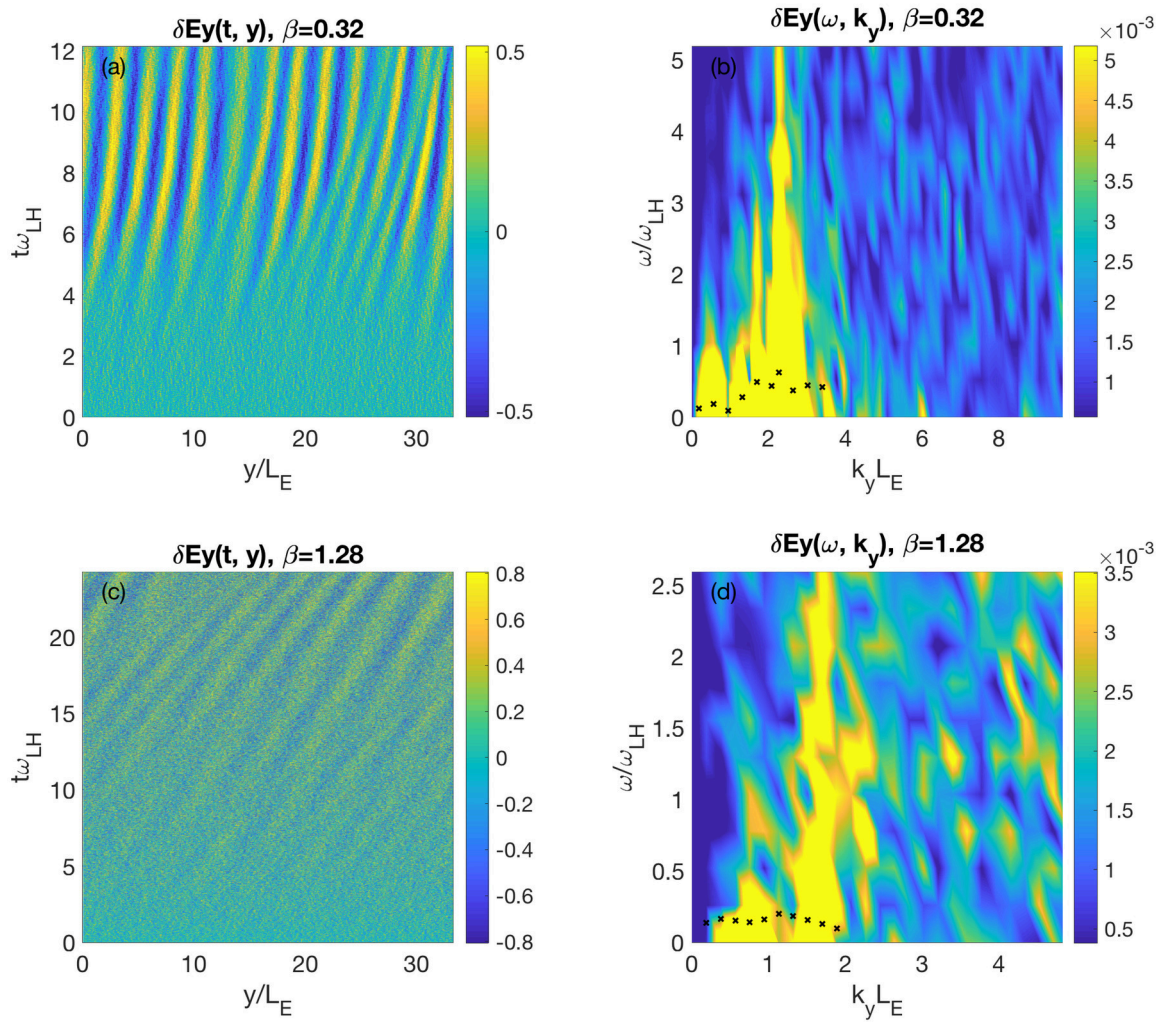
2019ja026815-f01-z-.eps



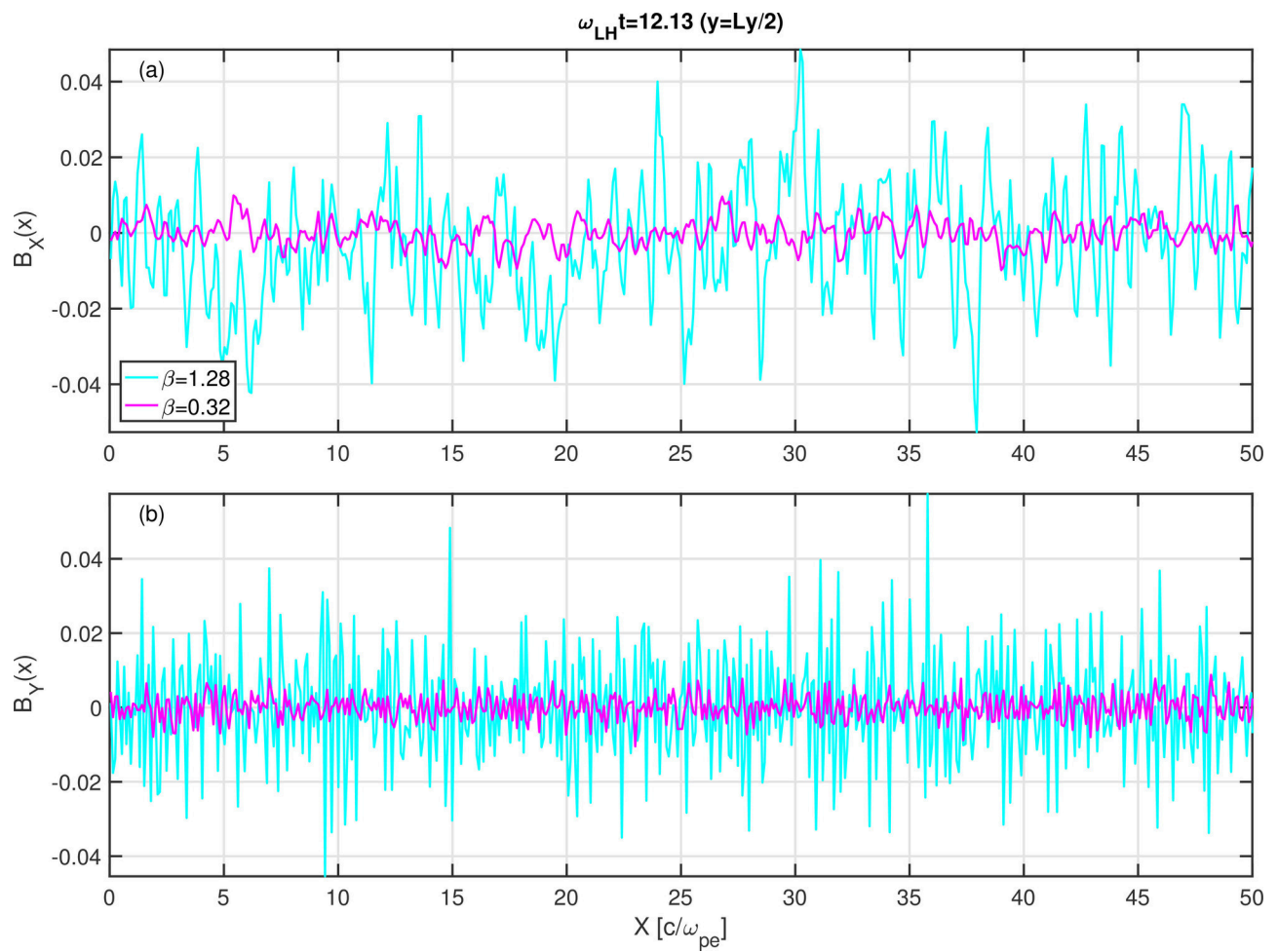
2019ja026815-f02-z-.eps



2019ja026815-f03-z-.eps



2019ja026815-f04-z-.eps



2019ja026815-f05-z-.eps